

# Water Resources Research®

## RESEARCH ARTICLE

10.1029/2022WR032536

## Insights Into the Dynamics of Vegetated Alternate Bars by Means of Flume Experiments

G. Calvani<sup>1,2</sup> , S. Francalanci<sup>1</sup> , and L. Solari<sup>1</sup> 

<sup>1</sup>Department of Civil and Environmental Engineering, University of Florence, Florence, Italy, <sup>2</sup>Hydraulic Platform LCH (IIC-ENAC), École Polytechnique Fédérale de Lausanne, Lausanne, Switzerland

### Key Points:

- The morphological alterations induced by vegetation establishment on riverbars depend on plant density
- Vegetation colonization increases the amplitude and wavelength of sediment deposits
- Vegetation establishment may enhance the bar-bend interaction and the planimetric response of the fluvial system

### Correspondence to:

G. Calvani,  
giulio.calvani@unifi.it

### Citation:

Calvani, G., Francalanci, S., & Solari, L. (2023). Insights into the dynamics of vegetated alternate bars by means of flume experiments. *Water Resources Research*, 59, e2022WR032536. <https://doi.org/10.1029/2022WR032536>

Received 21 APR 2022

Accepted 23 FEB 2023

**Abstract** Alternate bars are bedforms recognizable in straight or weakly curved channels as a result of riverbed instability. The length and height of alternate bars scale with the river width and the water depth, respectively. During low water stages, alternate bars become exposed and can be colonized by riparian vegetation. The effects of established plants on the morphodynamics of alternate bars have been poorly investigated. In this work, we focus on the effects induced by rigid vegetation on the dynamics and morphology of previously developed alternate bars in a straight channel by means of flume experiments. We investigate three different spatial densities of plants to reproduce scenarios of vegetation establishment. The results illustrate that vegetation alters both the altimetric and planimetric characteristics of bar patterns. In particular, as compared to bare-bed bars, vegetated bars have a higher wave amplitude and scour, and this effect becomes stronger with plant density. Moreover, they exhibit decreasing wavenumbers according to vegetation density. A comparison with previous fundamental work for the planimetric instability of straight channels with bare-bed alternate bars, suggests that the established vegetated bars may promote the transition to river meandering.

**Plain Language Summary** Vegetation is ubiquitous in rivers and plants may establish on the sediment deposits, called bars, that can be typically seen in rivers during low flows. Such deposits are accompanied by downstream scour regions and are commonly located according to an alternating pattern (left-right) along the sides of the river banks. The entire sequence of alternating deposits usually moves in the downstream direction, due to the action exerted by the flow. Surprisingly, the effects of vegetation on the geometrical features of sediment bars, as well as their dynamic properties, are still poorly investigated. Here, we present some controlled laboratory experiments whereby we initially reproduce sediment bars in a flume and later we mimic the establishment of vegetation on the sediment deposits according to different plant densities. Results illustrate that vegetation alters the sequence of sediment bars by increasing the scour depth and this effect becomes stronger with increasing plant density. Moreover, vegetated bars have a longer length of sediment deposit and a slower rate of movement, compared to bare-bed bars. By relying on a previous theoretical work on sediment bars, we suggest that longer and slowly-moving vegetated bars favor the transition of an initially straight channel toward a sinuous configuration.

## 1. Introduction

River bars are large-scale perturbations of the riverbed elevation commonly found in alluvial channels. They are typically characterized by the succession of longer and wider regions subjected to deposition and shorter and narrower areas subjected to deeper erosion with or without the presence of vegetation (Figures 1a and 1b). The main characteristic of river bars (i.e., the number of deposit/scour regions in a cross section) is defined by the bar mode,  $m$  (Crosato & Mosselman, 2009). According to its definition,  $m = 1$  identifies the configuration of alternate bars,  $m = 2$  corresponds to central bars, whereas higher values of  $m$  reflect the presence of multiple bars (e.g., multichannel systems). The formation of bars may be induced by the presence of either morphodynamic instabilities (Colombini et al., 1987; Engelund, 1970) or geometrical discontinuities (Blondeaux & Seminara, 1985; Tubino & Seminara, 1990), and are called either *free bars* or *forced bars*, respectively. Free bars appear as periodic waves over both the longitudinal and transverse directions (i.e., double harmonics) and typically migrate in the downstream direction (e.g., Colombini et al., 1987; Crosato et al., 2012; Rodrigues et al., 2012), whereas conditions for upstream migration are less common (Zolezzi et al., 2005). Forced bars do not migrate as their development and evolution are intrinsically related to the dynamics of the external forcing (Redolfi et al., 2019). Typical forced bars are located at the inner bank of river bends. Furthermore, past studies have shown that the presence of localized alteration of the channel geometry may affect the morphological characteristics of free

© 2023. The Authors.

This is an open access article under the terms of the [Creative Commons Attribution License](https://creativecommons.org/licenses/by/4.0/), which permits use, distribution and reproduction in any medium, provided the original work is properly cited.

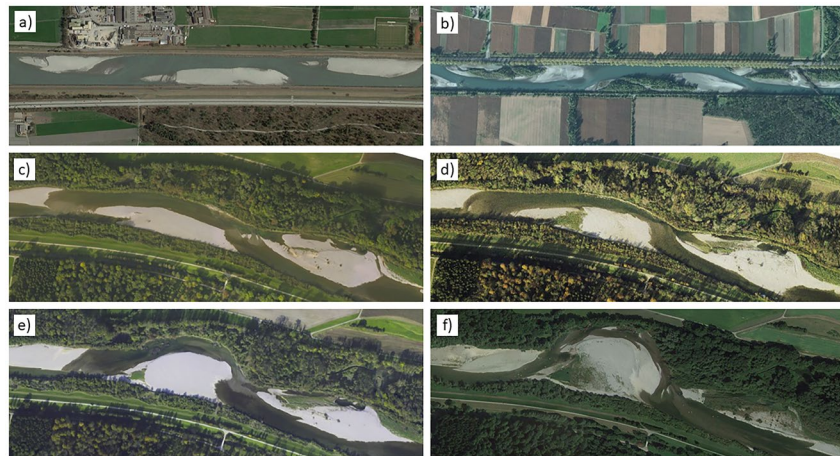


**Figure 1.** Morphological patterns in rivers with alternate bars and the temporal evolution of a reach of the Thur River after restoration (pictures a, b, f are from Google Earth, pictures c–e are courtesy of Paolo Perona). Flow is from right to left in all the panels. (a) Bare-bed alternate bars in the Rhine River near Vaduz, Liechtenstein; (b) Alternate bars with established vegetation in the Isère River near Grenoble, France; (c–f) The restored reach of the Thur River near Andelfingen, Switzerland: (c) Bare-bed alternate bars started forming (2006–2007); (d) Pioneer vegetation colonized bars and channel sinuosity increased (2009); (e) A steady bar encouraged erosion of the outer bank and a river bend developed (2010); (f) Bend evolution advanced (2012).

bars, in terms of the migration rate and bar wavelength (see Crosato & Mosselman, 2020, for a review). Previous works have referred to the resultant morphological bedforms as forced bars (Adami et al., 2016; Seminara & Tubino, 1992, among others), yet in more recent studies they have been called *hybrid bars* due to the mixed nature of free and forced mechanisms of formation (Duró et al., 2016).

The formation of free bars (either alternate or multiple) has been studied using the concept of a linear stability analysis. This mathematical tool allows for the identification of the bankfull aspect ratio, also known as the half-width-to-depth ratio, as the key parameter governing the conditions for the formation of alternate and multiple bar patterns (e.g., Colombini et al., 1987; Engelund, 1970; Ikeda, 1984). When the aspect ratio,  $\beta$ , is larger than a critical threshold,  $\beta_c$ , bed disturbances are naturally amplified and river bars start to develop. However, the intrinsic non-linear nature of bedform perturbations, due to the non-linear relationship in sediment transport formula, implies that the equilibrium morphology of such bedforms results from the superimposition of double-harmonic bed waves with different bar modes (Colombini et al., 1987). The contributions of bed-waves for different bar modes can be calculated through a Fourier analysis of the bed elevations (e.g., Zolezzi et al., 2005). Bar patterns have been widely investigated by taking into account the effects of heterogeneous bed sediment (Lanzoni & Tubino, 1999), unsteady flow conditions (Tubino, 1991), channel width variations (Zen et al., 2014) or suspended load (Federici & Seminara, 2006). Several studies tackled the problem through laboratory experiments (e.g., Lisle et al., 1991), field observations (e.g., Rodrigues et al., 2012) and numerical modeling (e.g., Defina, 2003).

Due to the alternating locations of scour and deposit regions, bar patterns (in particular alternate bars) represent a planimetric oscillatory system with a force applied periodically in space to the external banks (Crosato & Mosselman, 2009). When a system is subjected to a periodically applied force, the amplitude of its response depends on the frequency of the applied force. If this frequency is close or equal to a natural frequency of the system, the amplitude of the response tends, mathematically speaking, to infinity. In this case, the force and the system are described to be in *resonance* (Halliday et al., 2013). Resonance is a characteristic phenomenon which is present in many physical systems subjected to an oscillatory behavior, and it is well known to occur in acoustics and mechanics. However, it also emerges in many physical systems across a broad range of spatial scales, spanning from the infinitesimal world of quantum wave functions to the scale of satellite and planet orbits. In fluvial systems, resonance may occur either between the flow surface and the riverbed elevation (e.g., Andreotti et al., 2012) or between bedforms and planimetric patterns (e.g., Blondeaux & Seminara, 1985). In this work, we focus on the resonant conditions that occur between alternate bars and river bends. Such conditions may be expressed on the basis of channel curvature (Tubino & Seminara, 1990) and/or bank slope (Shimada et al., 2013), but hereafter we refer to the definition of resonant conditions in terms of the longitudinal

wavenumber (Blondeaux & Seminara, 1985). The longitudinal wavenumber,  $k_x$ , is proportional to the inverse of the longitudinal bar-wavelength scaled by the half-width of the channel, and, accordingly, it is a dimensionless quantity. If the bar wavenumber,  $k_x$ , is lower than the resonant value,  $k_{x,c}$ , the spatially alternating flow (due to the presence of bars) and the flow curvature originated by the planimetric pattern tend to reinforce each other, leading to the author-defined bar-bend resonance (Blondeaux & Seminara, 1985; Garcia & Niño, 1993). Bar-bend resonance increases outer-bank erosion and thus promotes the formation of meanders. When the two values,  $k_x$  and  $k_{x,c}$ , are equal, the resonance is maximized. Conversely, the bar-bend interaction sharply decreases for wavenumbers slightly higher than the resonant value, and for  $k_x$  higher than  $k_{x,c}$  no resonance occurs (Blondeaux & Seminara, 1985). While it is clear that forced and hybrid bars show longer wavelengths and are steady at equilibrium in comparison to free migrating bars, the mechanisms that cause bar-bend resonant conditions still remain unclear.

Riparian vegetation may colonize sediment bars (Figures 1c and 1d), provided that their root apparatus is strong enough to withstand hydrodynamic and sediment transport disturbances for a sufficiently long time (Calvani, Perona, et al., 2019; Perona & Crouzy, 2018). Established plants represent the most important living element affecting the morphodynamics of river corridors (Gurnell et al., 2012; Solari et al., 2016). For instance, Figures 1c–1f shows the temporal evolution of alternate bars in a restored reach of the Thur River (Schirmer et al., 2014). After restoration, free migrating alternate bars formed (Figure 1c), which were then being colonized by pioneer vegetation (Figure 1d). This vegetation stabilized bar migration and caused outer bank erosion and inner bank accretion, which, in turn, enhanced channel curvature and bend development. Figures 1c–1f suggests that bend development started after vegetation colonization. Therefore, it is clear that understanding the effects of vegetation on large-scale bedforms, as well as the dynamics of bars in terms of their stability and interactions with bends may lead to more effective river restoration projects.

The influence of vegetation on river bar dynamics has been investigated by field campaigns and numerical simulations to study the eco-morphodynamic interactions at different spatial and temporal scales. For instance, Serlet et al. (2018) monitored the evolution of alternate bars along the Isère River and showed that encroachment of vegetation on bare-bed surfaces can lead to non-migrating and longer bars. Similar conclusions were assessed by Bertoldi et al. (2014) and Jourdain et al. (2020) through numerical models. However, these studies also demonstrated that bars may keep migrating when vegetation is continuously removed during flood events. In other studies, laboratory experiments were performed to investigate the effects of vegetation on planform configuration. For instance, Tal and Paola (2010) carried out flume experiments with seeded *Medicago sativa* and found that the presence of roots may reduce morphological complexity (e.g., from a braided system to a single-thread channel). Real plants at different life stages were also involved in an experimental meandering channel by Kyuka et al. (2021). Rigid cylinders mimicking vegetation were used by Vargas-Luna et al. (2016) to investigate the effects of vegetation on the formation of alternate hybrid bars in a small-scale straight flume, whereas Rominger et al. (2010) studied the changes induced by added reed vegetation on a point bar in a previously shaped meandering channel. More recently, Vargas-Luna et al. (2019) performed large-scale laboratory investigations on the morphological alterations induced by adding low-flexible artificial grassy-type vegetation on bar topography. All of these studies found that vegetation effects may stabilize planform configurations. However, none of these studies investigated the mutual interactions between bar pattern and bend development in the presence of vegetation, nor did they consider different plant densities.

In this work, we present an experimental analysis aimed at providing quantitative evaluations of the effects induced by artificial vegetation on the dynamics of alternate hybrid bars with a particular focus on their height, celerity and interactions with bend resonance. We perform laboratory flume experiments where an initially plane bed, subjected to a constant flow rate, is allowed to evolve until a pattern of large-scale bedforms (e.g., bars) occurs. Then, artificial vegetation is deployed on the most exposed bar areas and the following hydraulic and bed changes are observed. The analysis shows that, after plant deployment, the amplitude of bar modes that are larger than one are damped, and the alternate bar pattern emerges. Additionally, we highlight that the wavenumber of vegetated bars is closer to the resonant value than that of the bare-bed conditions for all the tested configurations and vegetation densities. As a result, bar-bend resonance is promoted. Outcomes of the analysis are of particular interest for the design of improved river restoration projects and the definition of effective maintenance strategies of riparian vegetation.

**Table 1**  
*Experimental Conditions for Each Setup*

Setup	I	II	III	IV	V	VI
$Q$ ( $\text{l s}^{-1}$ )	3	3	3	3	3	3
$s$ (-)	0.009	0.009	0.009	0.008	0.008	0.008
$\rho_v$ ( $\text{stem m}^{-2}$ )	2,500	1,875	1,250	2,500	1,875	1,250
$a$ ( $\text{m}^{-1}$ )	2.5	1.88	1.25	2.5	1.88	1.25
$Y_0^a$ (cm)	1.7	1.7	1.7	1.8	1.8	1.8
$U_0^b$ ( $\text{m s}^{-1}$ )	0.40	0.40	0.4	0.39	0.39	0.39
$Fr^b$ (-)	0.98	0.98	0.98	0.94	0.94	0.94
$\beta^b$ (-)	12.9	12.9	12.9	12.2	12.2	12.2
$\beta_c$ (-)	8.5	8.5	8.5	8.2	8.2	8.2
$\theta^b$ (-)	0.0976	0.0976	0.0976	0.0919	0.0919	0.0919
$T_1$ (hr)	46	94	69	96	75	102
$T_2$ (hr)	22	37	24	20	26	20

Note.  $Q$  is the flow discharge,  $s$  is the bed slope,  $\rho_v$  is the vegetation density,  $a$  is the frontal area per unit volume,  $Y_0$  is the normal depth,  $U_0$  is the mean flow velocity,  $Fr$  is the Froude number,  $\beta$  is the aspect ratio,  $\beta_c$  is the threshold aspect ratio for bar instability,  $\theta$  is the Shields number,  $T_1$  is the duration of the first phase and  $T_2$  is the duration of the second phase.

<sup>a</sup>Quantity is measured. <sup>b</sup>Quantity is calculated from measurements.

## 2. Material and Methods

### 2.1. Experimental Setup and Procedure

Laboratory experiments were performed at the Fluvial Hydraulics Lab of the University of Florence in a 10.5 m long and 0.44 m wide straight channel with glass fixed walls and movable bed. The bed elevation at the downstream outlet was fixed by using a transverse wooden plate. The tilted flume was equipped with an adjustable recirculating pump, an upstream sediment feeder with frequency control and a downstream reservoir to dissipate water energy. The apparatus did not recirculate sediment. Instead, a double layer of non-woven fabric (mesh size equal to 105 micron) and a plastic net collected sediment at the downstream end of the flume and separated it from the water.

We designed our experiments to ideally obtain riverbed patterns of alternate bars, which can be colonized by vegetation during low flow periods (e.g., dry season in temperate climates). Poorly graded sand with mean grain size  $D_{50}$  equal to 0.95 mm (sorting index  $I = 0.5(D_{84}/D_{50} + D_{50}/D_{16}) = 2.15$ ) was selected for the bed material, based on the study of Vargas-Luna et al. (2016), and was used to feed the flume at the upstream inlet.

Experimental conditions were defined beforehand in terms of flow discharge,  $Q$ , and bed slope,  $s$ , according to the weakly non-linear theory of Colombini et al. (1987). In this regard, the theoretical threshold (in terms of aspect ratio) for the development of bar patterns ( $\beta_c$  in Table 1) was calculated by considering the coefficient of transverse sediment transport,  $r$ , equal to 0.3 (Colombini et al., 1987). Several tests were performed to identify the optimal combinations and to evaluate the effects of the presence or absence of a transverse plate at the inlet on the occurrence and characteristics of developed bars (Crosato et al., 2012). Such tests were also useful to calibrate the frequency controller of the sediment feeder, according to the formula of Wong and Parker (2006), which we found to be the best approximation of the sediment transport rates occurring in the flume for the different combinations of flow discharge and bed slope.

Each experiment started from an initial plane bed without vegetation. The upstream inlet was not equipped with a transverse plate (Crosato et al., 2012). Once the defined bed slope was set, a constant flow discharge was let run into the flume, along with the sediment feeding rate according to Wong and Parker's formula. As a result of free instability, alternate bars immediately started to appear (first phase, Figure 2a). For each setup (a combination of flow discharge and bed slope, see Table 1), the duration of the first phase was selected according to the downstream sediment transport rate and characteristics (size and celerity) of formed bars (48–72 hr, depending on the bed slope and the flow discharge setup). At this stage of the first phase, low flow passed over the bars and

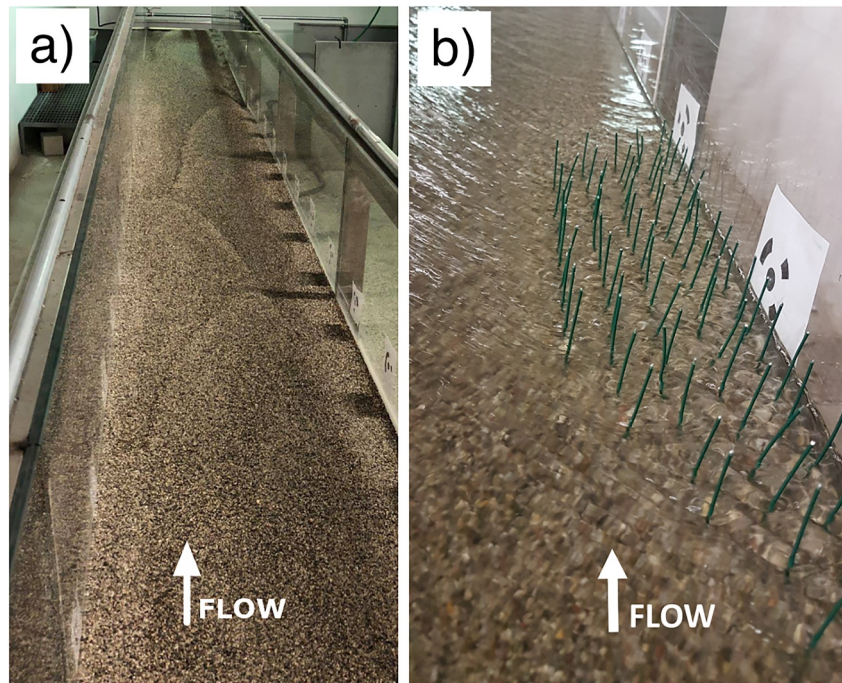


**Figure 2.** Alternate bars during an experimental run with and without vegetation. Markers used for Structure-from-Motion photogrammetry are visible on the right wall in both pictures. (a) Bare-bed alternate bars at the end of the run in one experimental day. Channel was dried to allow for surface scanning. (b) Artificial emergent vegetation deployed on top of already formed alternate bars.

so did the sediment transport, as bars were close to emergence, a condition where the bar top is close to the water surface. From free migrating bars, bedforms became non-migrating hybrid bars. We let the bare-bed configuration run for an additional 24 hr to reach sediment transport equilibrium conditions along the flume. We defined equilibrium as the condition when variation in the total sediment transport volume was lower than 5%, which roughly corresponds to an RMSE lower than 8 kg at the end of an eight-hour run (see Figure 3a for a measurement of downstream sediment transport). Slight differences in the duration of the first phase were considered among setups with the same initial conditions of flow discharge and bed slope (see Table 1).

Next, the second phase was initiated. Cylindrical metal rods with a stem diameter,  $D_v$ , equal to 0.001 m were manually deployed in a 0.3 m long and 0.08 m wide rectangular area on the higher and most downstream part of each deposition pattern, to resemble the position of pioneer plants in colonized river bars (e.g., Figure 1d). The deployment depth was set to 0.1 m, which we found to be deep enough to avoid the occurrence of uprooting events (Calvani, Francalanci, & Solari, 2019). Different densities of vegetation among experimental setups were obtained by varying the distance between metal rods and their number, keeping constant the deployment area. This results in different values of the frontal area per unit volume,  $a$  (Table 1). The highest vegetation density considered in the tests ( $\rho_v = 2,500 \text{ stem m}^{-2}$ , see Table 1) had the same frontal area per unit volume ( $a = \rho_v D_v = 2.5 \text{ m}^{-1}$ ) as previous experiments dealing with vegetation and bar morphodynamics (Vargas-Luna et al., 2019). According to the geometrical and mechanical properties of the metal rods, deployment of artificial cylinders was meant to simulate the colonization and establishment of mature plants (Hortobágyi et al., 2018; Vargas-Luna et al., 2016). We remark on scaling aspects in the Discussion.

Figure 2b shows one of the vegetated patches. Three scenarios of vegetation densities were studied in the experiments to investigate the effects of different strategies for vegetation maintenance (see Table 1). After vegetation deployment, water and sediment feeding were released under the same conditions of the first phase. The experiments were terminated 20–24 hr after vegetation deployment. The duration of the vegetated phase was set according to the observations made during preliminary experiments. After 20–24 hr of this phase, the edges of the bars started to be eroded. The scouring process began to affect the area where cylinder rods were placed, eventually leading to their removal. Although the uprooting of vegetation is a natural process in real rivers during high flood

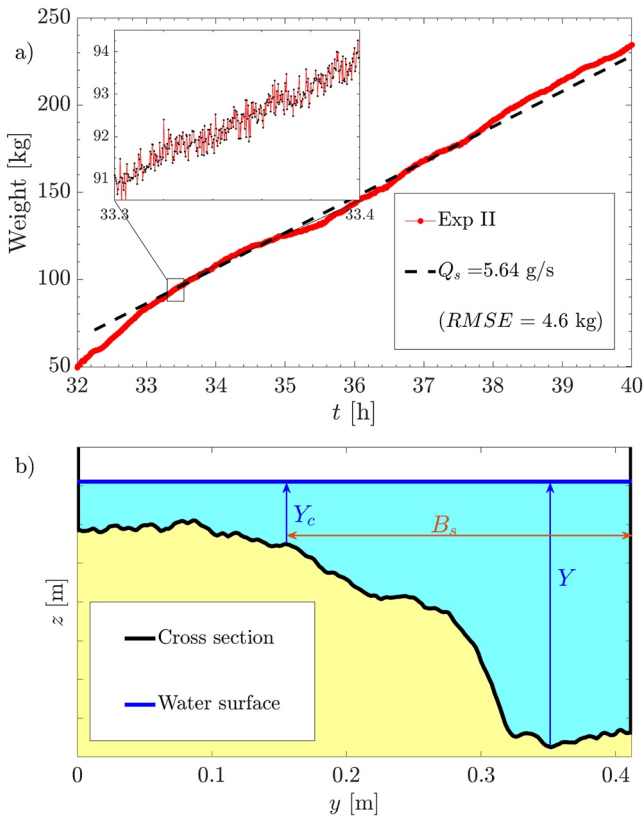


**Figure 3.** (a) Cumulative weight of sediment transported downstream versus time for the experiment II during the bare-bed phase. The dashed line shows the equilibrium sediment transport rate calculated by Wong and Parker's formula (2006). The inset panel highlights details at a finer temporal scale. (b) The cross section located at  $x = 5.5$  m of the experiment II at  $t = 40$  hr (see Figure 4a). The sketch shows the water depth,  $Y$ , the threshold water depth for sediment motion,  $Y_c$ , and the corresponding width,  $B_s$ , of the narrow sinuous channel.

events (Bywater-Reyes et al., 2015; Calvani, Francalanci, & Solari, 2019; Perona & Crouzy, 2018), the experimental setup and particularly the type of artificial vegetation were not meant to reproduce such a process.

## 2.2. Measurements and Data Analysis

At the beginning of each experiment, normal flow conditions were achieved in the central part of the flume (sufficiently far away from boundary inlet and outlet) in terms of water depth,  $Y_0$ , and flow velocity,  $U_0$ . These values are denoted by subscript 0 and reported in Table 1. During the experiments, we measured flow discharge using an ultrasonic flow meter located along the recirculating pipe. Downstream transported sediments were collected with a net and their weight was continuously monitored by four load cells (Figure 3a). At the end of each day, (i.e., 6–8 hr of run time), we let the water slowly flow out of the flume to dry the bed surface. A moving cart located above the channel was equipped with a downward-facing camera and a lighting system. We took sequences of 82 images of the channel bed and glass walls to include the placed markers in the pictures (see Figures 2a and 2b for markers on glass walls). Each picture overlapped the previous one by 80%, such that a marker was at least present in two consecutive pictures as required to perform a reliable Structure-from-Motion (SfM) analysis (Morgan et al., 2017). Each sequence of images was post-processed using the software Agisoft PhotoScan. First, the software created a 3D point cloud according to the coordinates of the marker center, and then it built a Digital Elevation Model (DEM) of the channel bed. The initial flat bed elevation was deducted from each DEM to highlight regions subjected to deposition or erosion. This is an ordinary procedure when dealing with the analysis of DEMs from flume experiments (Crosato et al., 2012; van de Lageweg et al., 2014). Accordingly, and for the sake of brevity, hereinafter we refer to DEM as the resulting elevation model from the subtraction procedure. In the rectangular grid of a DEM file, the columns represent cross sections of the flume, such that the distance between two consecutive cross sections is equal to the resolution of the DEM (i.e., 0.002 m). For the second phase, a DEM reconstruction procedure was conducted as in the case of the bare bar development (first phase) but it was instead performed every 4 hours. This time interval was defined in order to

accurately monitor the bed morphodynamic changes induced by artificial vegetation, while limiting the disturbances caused by the drying procedure. Accuracy of the DEM reconstruction was estimated to be 0.002 m along the vertical coordinate,  $z$ , and 0.001 m along both longitudinal,  $x$ , and transverse,  $y$ , directions.

For both phases of each experiment, we evaluated the longitudinal wavenumber,  $k_x$ , of the self-formed bar pattern. Based on the theory of Blondeaux and Seminara (1985), we considered the narrow sinuous channel flowing next to the regions subjected to deposition. In these parts of the channel, the flow is mostly directed longitudinally, and columns in the DEM files are more representative of the actual cross sections. From each DEM, we retrieved the width,  $B_s$ , of the narrow sinuous channel located next to the depositional patterns.  $B_s$  was considered to be the width of the active sediment transport flow area within the entire cross section (see Figure 3b). This width was limited on one side by the physical wall of the experimental flume, and on the other side by the point where flow depth,  $Y_c$ , satisfied the condition  $\theta = \theta_c$ , where  $\theta$  and  $\theta_c$  are the Shields and the critical Shields parameter for the initiation of sediment motion, respectively. As a result,  $Y_c$  can be calculated as

$$Y_c = \frac{\rho_s - \rho}{\rho} \frac{D_{50}}{s} \theta_c \quad (1)$$

where  $\rho_s$  and  $\rho$  are the sediment and water density, respectively, and the bed slope,  $s$ , corresponds to the longitudinal slope (Table 1). We considered  $\theta_c$  equal to 0.0495 (Wong & Parker, 2006). From the sinuous channel width,  $B_s$ , we calculated the corresponding aspect ratio of the sinuous channel as  $\beta_s = B_s/2Y$ , where  $Y$  is the water depth with

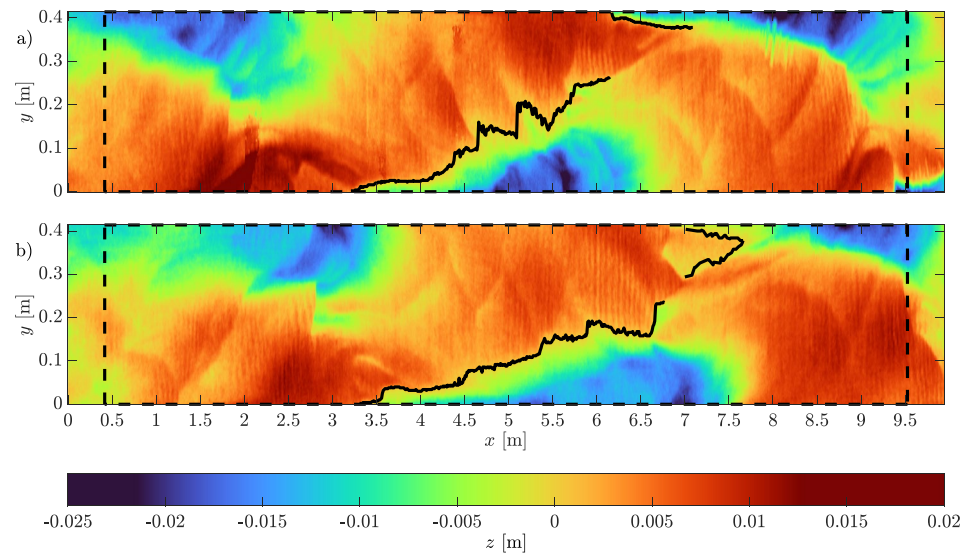


**Figure 4.** Two Digital Elevation Models of the experiment II ( $Q = 3$  l/s and  $s = 0.9\%$ ) during the initial phase without vegetation. Flow is from left to right. Black lines highlight the position of the bar fronts. The region within the dashed black lines was used for the analyses. Scale distortion is applied on the  $y$  axis. (a) Digital Elevation Model (DEM) after 40 hr (b) DEM after 46 hr.

respect to the thalweg of the cross section (Figure 3b). For each cross section of the sinuous channel, we calculated the longitudinal wavenumber,  $k_x$ , according to the formula proposed by Crosato and Mosselman (2009):

$$k_x = \frac{\beta_s}{4 \alpha C^2} \sqrt{4 \alpha (b + 1) - 1 - 4 \alpha^2 (b - 3)^2} \quad (2)$$

where  $C = 6 + 2.5 \log(Y / (2.5 D_{50}))$  is the Chézy coefficient and  $b = 2 \frac{\theta}{\partial \Phi}$  represents the degree of non-linearity in the sediment transport formula, and  $\Phi = q_s / \sqrt{\left( \frac{\rho_s - \rho}{\rho} g D_{50}^3 \right)}$  is the dimensionless sediment transport per unit width. For Wong and Parker's formula, the degree of non-linearity,  $b$ , is equal to  $3 \frac{\theta}{\theta - \theta_c}$ . In Equation 2,  $\alpha$  represents the ratio between the longitudinal and transverse adaptation lengths. According to Crosato and Mosselman (2009), it can be calculated as:

$$\alpha = \frac{3.4 \sqrt{\theta}}{\pi^2 C^2} \left( \frac{\beta_s}{m} \right)^2 \quad (3)$$

In each cross section, the bar mode,  $m$ , was calculated as the weighted mean among the first three bar modes (i.e.,  $m_i = 1, 2, 3$ ) and the null mode (i.e.,  $m_i = 0$ ), which corresponds to a flat cross section. The weighted mean was calculated according to the squared amplitude of each mode, as:

$$m = \frac{\sum_{i=0}^3 m_i A_i^2}{\sum_{i=0}^3 A_i^2} \quad (4)$$

where the amplitude  $A_i$  of each bar mode,  $m_i$ , was calculated by means of a Fast Fourier Transform (FFT) analysis applied to each cross section. The wavenumber of the entire sinuous channel was then calculated by averaging the values obtained in each cross section of the DEMs. Based on the theory of Blondeaux and Seminara (1985), we graphically compared the wavenumbers of the bar patterns to the resonance value,  $k_{x,c}$ , for the bend instability toward meanders. The cumbersome expression of the bar-bend resonant wavenumber,  $k_{x,c}$ , is reported in the Appendix. Herein, we want to recall the important role that is played by the transverse sediment transport coefficient,  $r$  (e.g., Colombini et al., 1987; Engelund, 1970). For the sake of a sensitivity analysis, we considered different values of the transverse sediment transport coefficient,  $r$ , in the range 0.3–0.6. Values of  $r$  equal to 0.5–0.6 are typical for a stability analysis of large scale bedforms (Bärenbold et al., 2016; Blondeaux & Seminara, 1985), whereas Colombini et al. (1987) suggested  $r = 0.3$  for better comparison with experimental measurements.

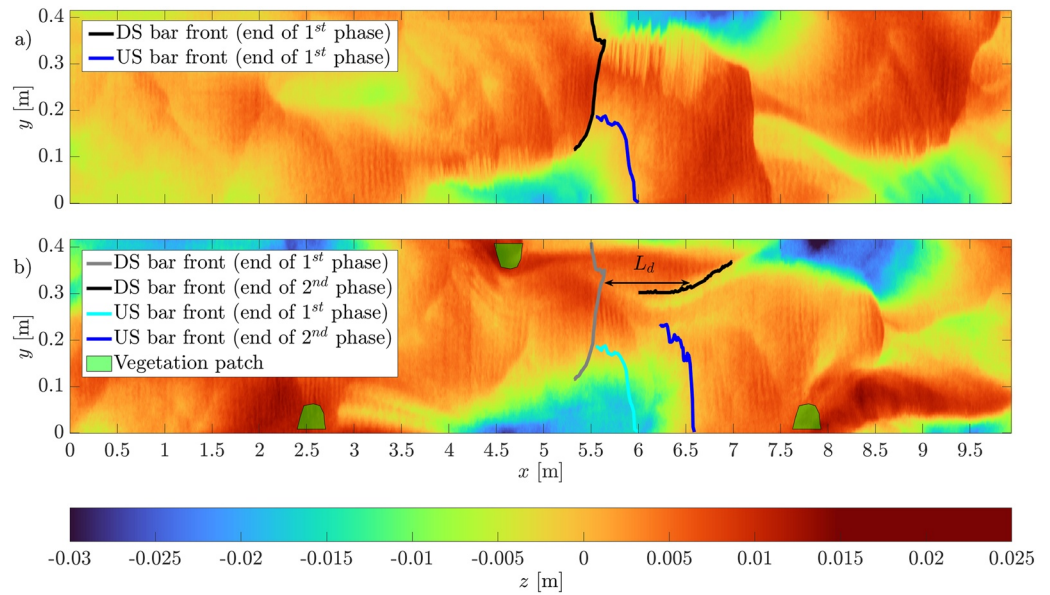


**Figure 5.** The procedure used to calculate the length of the deposit downstream of the vegetation patch in the Digital Elevation Models (DEMs) of the experiment II. Flow is from left to right in both the panels. DS and US stand for downstream and upstream, respectively. (a) DEM at the end of the bare-bed phase. The black and blue lines display the position of the DS and US bar fronts, respectively. (b) The DEM 16 hr after vegetation deployment. Locations of vegetation patches are highlighted by green polygons. The gray and cyan lines indicate the DS and US bar fronts at the end of the first phase. The black and blue lines highlight the location of the deposit and the US bar front, respectively.  $L_d$  shows the length of sediment deposit downstream of the artificial patch of vegetation.

Moreover, we performed additional analyses for each DEM. Each analysis was carried out for a reduced length of the DEMs; a length equal to the flume width was removed both at the upstream and at the downstream parts of the DEMs (see the region delineated by dashed black lines in Figure 4), to avoid the possible influences induced by the upstream and the downstream boundary conditions. We calculated the average longitudinal slope, bar height (i.e., amplitude) and areal distribution of scour and deposition with respect to mean bed level (i.e.,  $z = 0$ ) to investigate whether net global deposition or erosion took place during the run. We considered the dimensionless bed elevation,  $\tilde{z}$ , to plot the areal distribution:

$$\tilde{z} = \frac{z - z_{\min}}{z_{\max} - z_{\min}} \quad (5)$$

where  $z_{\min}$  and  $z_{\max}$  refer to the minimum and maximum bed elevation in each DEM, respectively. Bar amplitude,  $\Delta a$ , was calculated, by definition, as the difference between the highest and the lowest points in the same cross section. As a reference value for the bare-bed configuration at the end of the first phase, we considered the maximum  $\Delta a$  evaluated among all the cross sections. Additionally, we used the DEMs to calculate the celerity of bars. For this purpose, bar fronts of the same bar were highlighted in two consecutive DEMs (continuous black lines in Figure 4). We defined bar fronts as the locations where the bed elevation was equal to the mean bed level with respect to the smoothed initial conditions (i.e.,  $z = 0$ ). As such, only the points along the front line that were present in both of the consecutive DEMs were included in the calculations. Additionally, for  $y$ -coordinates showing more than one point on the front line, we took into account only the most upstream location. Then, bar celerity was calculated as the average downstream shift of the entire front line over time.

For the DEMs of the second phase (i.e., after vegetation deployment) we measured the length  $L_d$  of the deposited region downstream of the second patch of vegetation (Figure 5), to avoid the influence of inlet and outlet boundary conditions on the most upstream and most downstream patches, respectively. The length of the downstream deposit was measured as the downstream shift of the front bar, which is similar to the procedure used to measure the celerity of bars (see Figure 4 for comparison). An uncertainty of  $\pm 3$  cm was accounted for in the measurements. The measured length was then compared to the value predicted by the theory proposed in Zong and Nepf (2011) and Follett and Nepf (2012). The authors found that the deposit length can be interpreted as the sum

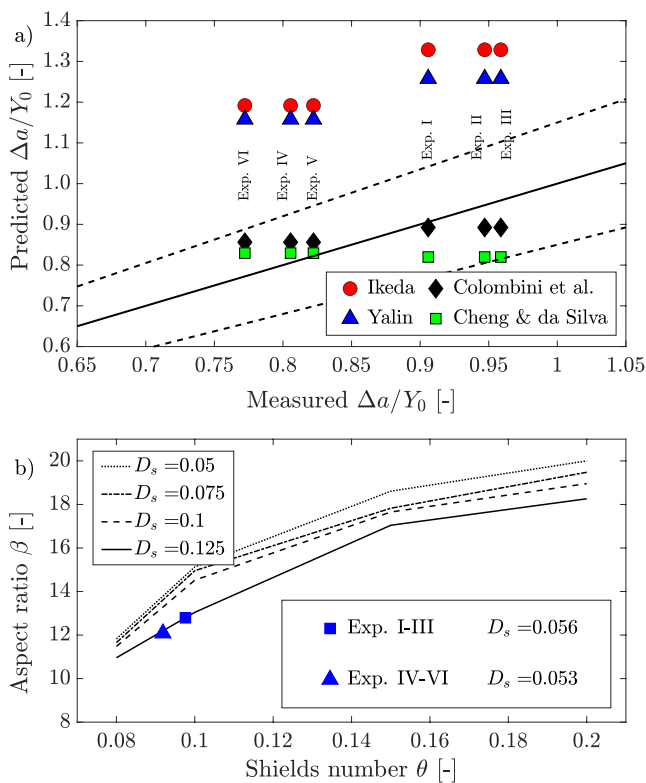


**Figure 6.** Comparison of experimental data against theoretical values for the bars at the end of the first phase (bare-bed conditions). (a) Predicted versus measured dimensionless bar height for the performed experiments. Values are scaled by normal water depth,  $Y_0$ . Different formulas for predicted values are used (Cheng & da Silva, 2019; Colombini et al., 1987; Ikeda, 1984; Yalin, 1992). The continuous black line represents the line of perfect agreement, whereas the dashed lines accounts for  $\pm 15\%$  error. (b) Aspect ratio  $\beta$  compared to Shields number  $\theta$  for the critical conditions of bar emergence. Theoretical curves are plotted for different values of the dimensionless grain size,  $D_s = D_{50}/Y_0$  (Vignoli & Tubino, 2004). The points refer to experimental data in bare-bed conditions (first phase, see Table 1).

condition (called bar emergence), very low sediment transport took place over the bar top. The experimental data reasonably agree with the critical conditions for bar emergence numerically found by Vignoli and Tubino (2004) (Figure 6b).

### 3.2. Vegetated Conditions (Second Phase)

During the second phase of the experimental run, artificial vegetation (i.e., metal rods) was present on top of the self-developed bars. Vegetation strongly affected the flow field and the sediment transport at the local (patch) and reach (bar) scales, even with the lower tested density ( $\rho_v = 1,250 \text{ stem m}^{-2}$ ). During the run of the second phase, we observed an increased flow diversion toward the area opposite of the deposited region. Because of conditions close to bar emergence, flow velocity on top of the bars was lower than the mean flow velocity, even at the end of the first phase. However, the presence of vegetation further decreased flow velocity in such regions. These observations are consistent with laboratory experiments on flow through vegetated patches (e.g., Follett & Nepf, 2012; Vargas-Luna et al., 2016; Zong & Nepf, 2010), with experiments with alternate vegetated patches (e.g., Bennett et al., 2002; Rominger et al., 2010) and with numerical simulations on vegetated alternate bars (e.g., Jourdain et al., 2020).

Lower flow velocities within the vegetated patch led to additional grain deposition on the bar top. At the same time, higher flow velocities in the opposite region significantly increased erosion in these regions. As a result,

of the lengths of the *steady wake region* and the *wake recovery region* which form downstream of a vegetation patch. The flow velocity within the artificial plants was estimated according to the relationship proposed by Rominger and Nepf (2011). In this case, an uncertainty of  $\pm 20\%$  was accounted for in the estimation of the friction velocity on the bar top (Bentham & Britter, 2003).

## 3. Results

### 3.1. Bare-Bed Conditions (First Phase)

Results from the first phase (i.e., the bare-bed configuration) showed that large scale bedforms, easily identifiable as alternate bars (see Figure 2a), started developing immediately (i.e., after the first couple of hours of the run), due to bed instability (i.e.,  $\beta > \beta_c$  for all the setup, see Table 1). As predicted by linear theory (Colombini et al., 1987), during the first phase we observed self-formed bedforms migrating downstream. After the initial bed instability and appearance of free migrating bars, bedforms started growing in wavelength and amplitude. Wavelength growth was observed to occur during the first 24 hr of the run, while bar height (i.e., amplitude,  $\Delta a$ ) continued to increase for a longer period (40–56 hr) as a result of deposition on the top and erosion in the pool. These observations are comparable to previous experimental works on large-scale bedforms (e.g., Crosato et al., 2012; Lanzoni, 2000a, 2000b; Lisle et al., 1991; Vargas-Luna et al., 2019), and are consistent with the development of hybrid bars from free migrating bedforms (Crosato & Mosselman, 2020; Duró et al., 2016). In Figure 6a, we compare the measured dimensionless bar amplitude ( $\Delta a/Y_0$ ) against the values predicted by different formulations available in literature. The comparison shows agreement between the predicted and measured values for the empirical formula of Cheng and da Silva (2019) and the theoretical relationship derived by Colombini et al. (1987) (Figure 6a).

The deposition process reduced the water depth on the top of the bars and small-scale bedforms (i.e., ripples) started developing, due to the smaller depth-to-sediment ratio locally occurring on the bar top (i.e.,  $\theta$ -to- $\theta_c$  ratio, see Colombini and Stocchino (2011) for some insights into the formation of ripples). The presence of small-scale bedforms on the deposited regions was evident in all of the setups. The deposition of sediment continued to occur until the bar top was close to the water surface (60–72 hr into the run). In this

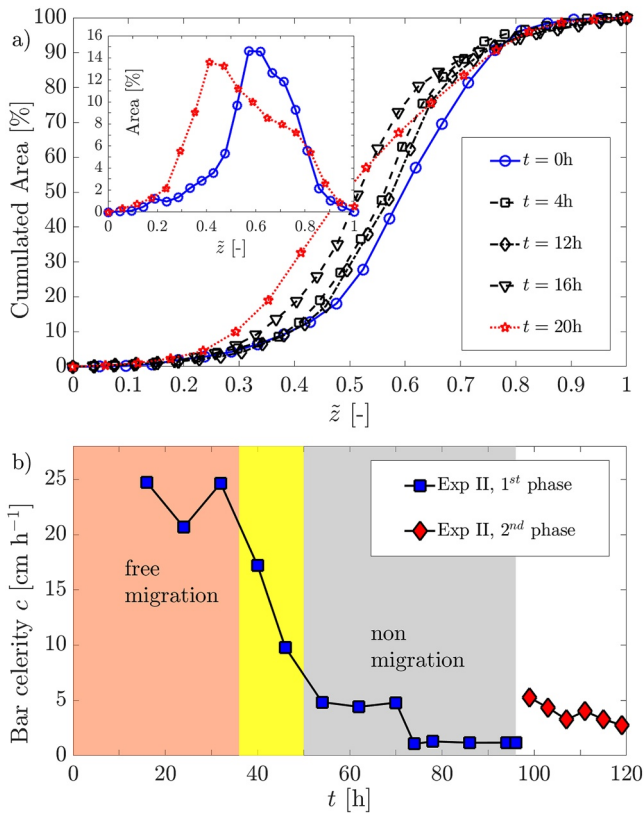


**Figure 7.** Comparison between bare-bed and vegetated conditions in terms of areal distribution and bar migration rate. (a) Dimensionless cumulative distribution of area above a certain dimensionless bed elevation  $\tilde{z}$  in the experiment V. In the inset panel, the dimensionless distribution of area during the vegetated phase. Time  $t = 0$  hr refers to deployment of vegetation; (b) Bar celerity (migration rate) versus time for the first phase (blue points) and second phase (red points) of the experiment II. The shaded yellow region highlights the transition from free migrating (orange) to almost steady (gray) bars.

bar amplitude continued to grow during the second phase and areal distribution of the bar tops and pools changed because of the different size of regions where deposition or erosion took place. Changes in areal distribution are shown in Figure 7a for the experiment V, where dimensionless cumulative area is plotted against the dimensionless bed elevation  $\tilde{z}$  (Equation 5). The blue and red lines refer to the dimensionless areal distribution (the area above a certain bed elevation  $\tilde{z}$ ) at the end of the first and the second phase, respectively. At the end of the first phase (blue line), only 20% of the area was lower than 50% of the bed elevation ( $\tilde{z} = 0.5$ ), whereas the area below  $\tilde{z} = 0.5$  is larger than 50%, at the end of the second phase (red curve). Yet, 90% of the spatial area is found to be below 75% and 65% of the bed elevation range ( $\tilde{z} = 0.65 - 0.75$ ), in the bare-bed and vegetated configurations, respectively. Additionally, the inset panel of Figure 7a clearly shows that the maximum of the distribution shifts toward lower bed elevations (e.g., from  $\tilde{z} = 0.6$  to  $\tilde{z} = 0.4$ ). As a result, the depositional areas showed a considerable contraction, whereas areas influenced by scouring processes became wider. This is particularly evident when comparing a DEM at the end of the first phase (Figure 5a) to a DEM of the second phase (Figure 5b), where the extension of green and blue regions showing erosion patterns enlarges and becomes deeper in the second phase.

The evolution from free migrating to hybrid bars is evident when looking at the blue points in Figure 7b. Values of bar celerity during the initial part of the first phase (yellow area in Figure 7b) highlights the presence of free migrating bedforms. After that, bar migration started slowing down (gray area in Figure 7b). The yellow overlapping region between the orange and gray areas approximately shows the time for the transition from free migrating to steady bars. At the end of the bare-bed stage (first phase), hybrid bars were almost steady. As soon as the run of the second phase began, we observed bars re-starting migration in the downstream direction (red points in Figure 7b). Bar migration occurred due to the downstream shift of both the upstream and the downstream fronts (Figure 5b). However, because the displacement of the downstream front was longer than that of the upstream one, the bars changed both in position (i.e., migration) and length (i.e., elongation). Both of the processes occurred at the same time and more rapidly during the first 12 hr of the run, for all the configurations of stem density. In terms of bar celerity, the rate was larger than the migration rate at the end of the first phase (red points in Figure 7b).

The comparison between the measured and the predicted length of the sediment deposit downstream of the vegetation patch is displayed in Figure 8 for all tested experimental conditions and vegetation densities. The results are plotted in terms of the dimensionless length of the deposit,  $L_d/B$ , where  $B$  is the flume width. Figure 8 shows satisfactory agreement between the measured and the predicted values with a maximum error of 15% in setup I ( $Q = 3$  l/s,  $s = 0.8\%$ ,  $\rho_v = 2,500$  stem  $m^{-2}$ , see Table 1). It is important to note that the analysis of the root mean square error reveals that the prediction is more accurate (RMSE = 0.129) for setups IV–VI (diamond points in Figure 8) than for setups I–III (RMSE = 0.173). According to the vegetation density, the lowest prediction error is for the highest tested density (RMSE = 0.133) and the highest error was observed for the lowest vegetation density (RMSE = 0.168). The mid-range vegetation density exhibits an error between the two (RMSE = 0.155).

Figure 9 shows the results of the analysis performed on the longitudinal wavenumber,  $k_x$ . For each experimental setup, boxplots represent the distribution of the wavenumbers in each phase, calculated using Equation 2. For each phase (i.e., bare-bed or vegetated), the boxes in each panel contain values from the 25th to the 75th percentiles of the wavenumber distribution, and the horizontal line in each box represents the mean value. Whiskers extend to the outermost point within the range  $\pm 3\sigma$  (with  $\sigma$  the distribution standard deviation). Wavenumbers outside of the whiskers are considered outliers and are represented by black stars. Horizontal black lines show the critical values for the bar-bend resonant condition, according to the theory of Blondeaux and Seminara (1985).

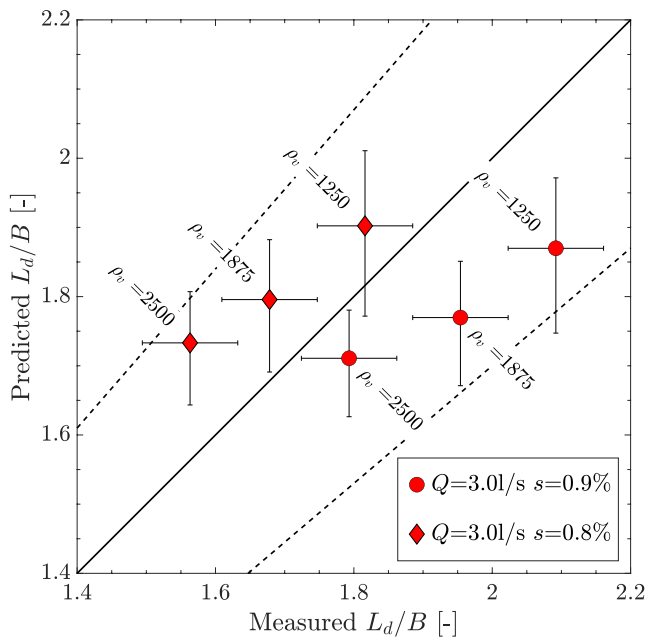


**Figure 8.** Comparison between the predicted and measured length of the sediment deposit,  $L_d$ , downstream of the vegetation patch at the end of the second phase. The predicted values are calculated according to Follett and Nepf (2012). Values are made dimensionless using the channel width,  $B$ . The line of perfect agreement (continuous black line) and the line of  $\pm 15\%$  error (dashed black line) are also shown.

For comparison, we show the critical threshold,  $k_{x,c}$ , for all tested values of the coefficient  $r$  for the transverse sediment transport. Due to the highly non-linear effects displayed by the lateral sediment transport coefficient, thresholds for  $r = 0.3-0.5$  are similar in setups I–III (panel a–c in Figure 9), whereas they are slightly different in setups IV–VI (panel d–f).

The results of the analysis show some small differences ( $t$ -Student test: minimum  $p$ -value = 0.78 with statistical significance equal to 0.05) in the distribution of the wavenumbers for the bare-bed stage (first phase) in setups with equal initial conditions (setup I–III and IV–VI). This could be due to small perturbations during the initial free bed instability which may have affected the wavelengths of the subsequent hybrid bars. Nevertheless, average values of the distributions are still similar among equal setups (in Figure 9, compare lines corresponding to the mean value among panels a–c for setups I–III and among panels d–f for setups IV–VI). Bar wavenumbers are lower in setups IV–VI than in setups I–III in both phases. This result is in agreement with the theory of bare-bed bars (e.g., Colombini et al., 1987) but is also confirmed for the bedforms after plant deployment (second phase) with the exception of setup II (Figure 9b). Results of this analysis show that the wavenumbers,  $k_x$ , in bare-bed conditions (i.e., first phase) are higher than the resonant values in most of the setups. Only setup II and III show values in the tail of the distribution which are close to the critical value corresponding to  $r = 0.6$  (the dotted line in Figures 9b and 9c). However, for these runs, the average value is well above the resonant conditions for all the tested  $r$  coefficients. Conversely, bar patterns during the vegetated phase exhibit wavenumbers much closer to or lower than the threshold in all the tested configurations except setup II (Figure 9b). Furthermore, the bar wavenumbers after plant deployment decrease according to the vegetation density value, except setup III (Figure 9c).

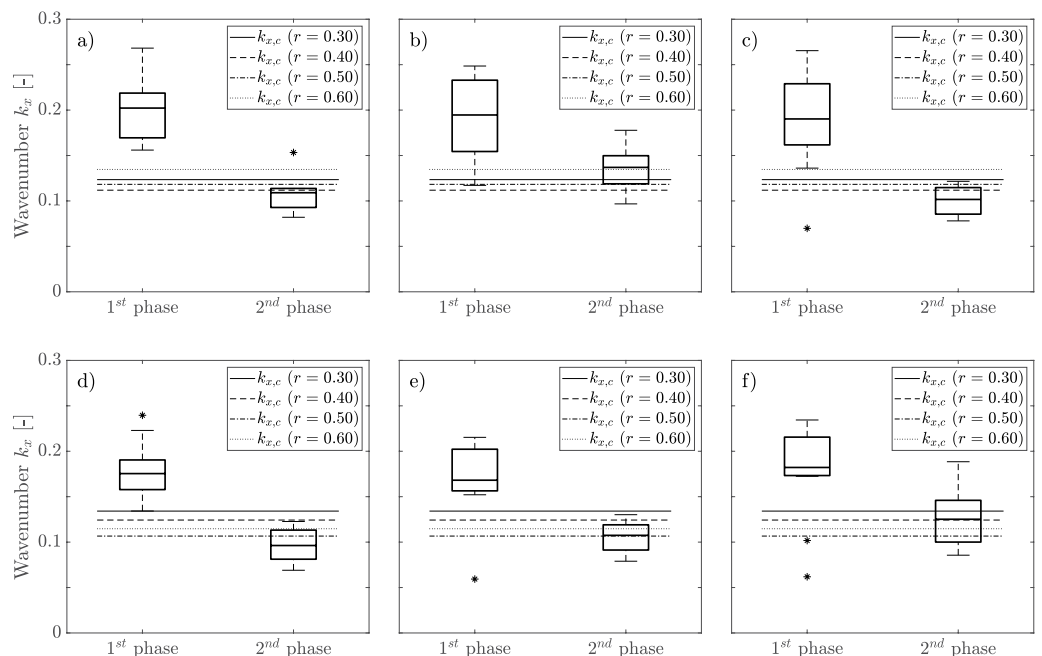


**Figure 9.** Boxplots of the wavenumber distributions and comparison to resonant value,  $k_{x,c}$ , according to different values of the transverse sediment transport coefficient,  $r$ , for both the bare-bed and vegetated phases. Boxes extend from 25th to 75th percentiles of the distributions of bar wavenumbers. Horizontal line in the boxes represents the mean value. Whiskers extend to  $3\sigma$  and stars represent outliers. (a) Setup I; (b) Setup II; (c) Setup III; (d) Setup IV; (e) Setup V; (f) Setup VI.

## 4. Discussion

### 4.1. Scaling Aspects

In flume experiments, the appropriate inclusion of scale aspects is always important to design the experimental setup and to properly understand results and outcomes. However, while scale issues can be tackled fairly easily when dealing with flow conditions only (fixed-bed without plants), the problem becomes more complex after adding sediment transport and aquatic and/or riparian vegetation into the experiment.

As such, the scaling of unvegetated experimental results with mobile-bed conditions can be addressed with relative ease by taking into account the dimensionless Shields parameter,  $\theta$ . Consequently, the downscaling of a real river to an experimental run may result in the use of a different, and often smaller, grain size to obtain similar results (e.g., Vargas-Luna et al., 2019). Therefore, flume experiments with sand-bed material are often representative of gravel-bed river processes in terms of sediment transport rate and bed topography (e.g., river bars). Moreover, up-scaling the results of such experiments requires the formation of similar large-scale bedforms of the same mode (e.g., bar mode  $m$ ) (Crosato & Mosselman, 2020; Kleinhans et al., 2014). Additionally, the formation of large-scale bedforms may alter the sediment transport and the evolution of the system toward different patterns of bed topography (Francalanci et al., 2012).

While the use of mobile-bed conditions in flume experiments is a common practice, representing the effects of vegetation is still challenging. Despite the recent efforts to understand the mutual interactions between vegetation, flow and sediment transport, scaling such interactions remains an open question, due to the different and wide temporal and spatial scales involved in the processes (Calvani, Perona, et al., 2019; Solari et al., 2016; Yamasaki et al., 2021). Many studies involved *Medicago sativa* sprouts to properly affect hydrodynamics due to the presence of foliage. However, the root apparatus may uncontrollably alter sediment entrainment and bank stability (Bertoldi et al., 2015; Kyuka et al., 2021; Rominger et al., 2010; Tal & Paola, 2010). Few studies have used real vegetation in full-scale channels (e.g., Berends et al., 2020). Conversely, many studies have used artificial plants, often represented by rigid cylinders (Bennett et al., 2002; Follett & Nepf, 2012; Vargas-Luna et al., 2016; Zong & Nepf, 2010) or flexible plastic plants (Vargas-Luna et al., 2019) to mimic the main alteration induced on hydrodynamics. In this study, the deployment of artificial metal rods was mainly meant to promote flow diversion on bar tops during the run of our experiments and the experimental observations were in agreement with previous laboratory investigations (Bennett et al., 2002; Rominger et al., 2010; Vargas-Luna et al., 2016).

We designed our experiments to reproduce the formation of free alternate bars and their evolution as steady hybrid bars altered by the colonization of emergent rigid vegetation. Although the experimental setup was meant to investigate such processes, it was not designed to be a scaled reproduction of any existing river. Stem diameter was chosen in order to avoid scour around stems due to a sediment-to-stem ratio lower than 1 (Melville & Sutherland, 1988), whereas values of frontal area per unit volume ( $a$  in Table 1) are in the range analyzed by Bennett et al. (2002). Scaling and extrapolating results to real cases is still challenging due to the unknown effects induced by the above- and the below-ground parts of the vegetation on the sediment. Nevertheless, the experimental findings are consistent with those observed in typical gravel-bed rivers where vegetation establishes on exposed deposits (Adami et al., 2016; Hortobágyi et al., 2018; Serlet et al., 2018).

### 4.2. Experimental Setup

In our experimental facility, alternate bars started developing without the use of a transverse plate, but instead as a result of free bed instability. The use of transverse plates is a common practice in flume experiments (e.g., Crosato et al., 2012; Lanzoni, 2000a, 2000b; Lisle et al., 1991; Venditti et al., 2012) because it allows for faster development of alternate bars (e.g., Vargas-Luna et al., 2019). However, a side effect is that the formation of non-migrating large-scale bedforms (i.e., hybrid bars, according to Duró et al. (2016)) starts right at the beginning of the experiment. Free bed instability allows for the formation of migrating bars, at least for a certain amount of time. In our experiments, the free migration lasted for approximately 40 hr (see Figure 7b). Then, the presence of non-uniform conditions (e.g., sediment heterogeneity (Lanzoni, 2000b)) and boundary conditions (e.g., the finite length of the flume) affected the migrating rate and turned free bars into hybrid bars (Crosato & Mosselman, 2020; Duró et al., 2016). The total duration of the first phase (bare-bed conditions) is similar to other experiments with and without artificial vegetation (e.g., Lanzoni, 2000b; Vargas-Luna et al., 2019).

At the end of the first phase (bare-bed conditions), bar migration was almost negligible and no changes occurred in amplitude (Figure 7b). Duration of the second phase (20–24 hr) was set according to observations of eco-morphodynamic processes occurring after vegetation deployment in preliminary tests. We observed that, after 20–24 hr, scouring could take place at the leading edge of the bar, thus extending to the most central row of artificial stems, eventually promoting plant removal. Although morphodynamic changes may potentially take place for longer experimental durations (e.g., Crosato et al., 2012), our flume experiments were not meant to simulate processes of vegetation uprooting due to bed scour. Plant root apparatus was not properly modeled by the artificial rods (Vargas-Luna et al., 2016) and bed erosion is a relevant factor affecting the uprooting process of plants in natural vegetated rivers (Bywater-Reyes et al., 2015; Calvani, Francalanci, & Solari, 2019).

For a better comparison between bare-bed and vegetated scenarios, a setup without vegetation could have been conducted for a duration equal to the sum of first and second phases. This type of “blank” case has been recently carried out by Vargas-Luna et al. (2019), among others. However, past studies highlight that significant changes in the morphology of steady hybrid bars occur over long time scales only (~1 week, according to Crosato et al. (2012)). In our case, the difference in duration was a maximum of 24 hr (i.e., the duration of the second phase). Other studies have considered the steadiness and almost emergent conditions of hybrid bars as an equilibrium condition in similar experiments, even with shorter duration of the bare-bed phase (Lanzoni, 2000b; Lisle et al., 1991; Nelson & Morgan, 2018). We cannot guarantee that small changes would not have taken place in the flume during the time left to achieve the full equilibrium duration of bare-bed conditions. Nevertheless, it is clear that the difference in duration is much less than the time scale for morphological changes shown in the literature.

#### 4.3. Bar Migration and Amplitude

We can interpret the bar migration-elongation process in two different ways. On one hand, it can reasonably be considered as the adjustment of the large-scale bedforms to the altered configuration, after vegetation deployment. On the other hand, the concurrent migration-elongation process may be explained by the formation of a sediment deposit downstream of the vegetated patch (Follett & Nepf, 2012; Zong & Nepf, 2010, 2011). Simultaneously, this deposit may have pushed the upstream front of the next downstream bar pattern. This process is similar to the bar-push mechanism in meander bends (e.g., van de Lageweg et al., 2014). In the analysis of the length of the deposit downstream of the vegetated patch (Figure 8), we accounted for the uncertainty related to the application of Follett and Nepf's relationship. Their theory was developed for a vegetated patch located at the center of the channel, whereas in our experiments vegetated patches were located near the lateral wall. This may have induced some effects on the flow velocities within the stems, thus altering the structure and size of the downstream deposit (Nepf, 2012). Nevertheless, the comparison well supports the idea of non-migrating vegetated bars as opposed to the temporary migration, which is also consistent with field measurements (e.g., Adami et al., 2016; Serlet et al., 2018) and numerical simulations (e.g., Jourdain et al., 2020). Furthermore, experiments with the same hydraulic conditions (the same marker in Figure 8) but different vegetation densities show that the lower the density of vegetation, the shorter the measured length of the downstream deposit. This finding is in agreement with theoretical formulations available in the literature (Follett & Nepf, 2012; Zong & Nepf, 2011). Vegetation density also influences the time evolution of the sediment deposit which appears to form faster in the setups with the high vegetation density in comparison to those with lower densities (Table 2). The bed slope appears to have a positive effect on the initial development of the sediment deposit, as the setups with higher bed slopes (I–III) show a high migration rate in the vegetated phase (compare values of  $c$  in Table 2).

A similar correlation can be made for the bar amplitude (Table 2), but the effects of slope appear to be more subtle. A clearer trend is shown for the plant density, with the highest bar amplitudes occurring in the experiments carried out with the highest vegetation density, and vice versa. Measurements of the dimensionless cumulative distribution of spatial area are consistent with previous experimental observations (Rominger et al., 2010) and numerical simulations (Jourdain et al., 2020). Particularly, the shift of the peak in the areal distribution from higher bed elevations toward lower bed elevations (see inset panel in Figure 7a) was also obtained by Bertoldi et al. (2014) in numerical simulations by including vegetation dynamics (i.e., plant growth and removal due to uprooting). The change in the dimensionless areal distribution was also found by Bertoldi et al. (2011) in field observations on braided rivers and was identified as a topographic signature of the processes related to plant colonization and development.

**Table 2**  
*Experimental Results for Both Bare-Bed (First Phase) and Vegetated (Second Phase) Configuration*

Setup	I	II	III	IV	V	VI
$c$ (1st phase) (cm h <sup>-1</sup> )	22.3	24.7	24.2	22.6	21.1	21.8
$c$ (2nd phase) (cm h <sup>-1</sup> )	5.7	6.2	6.6	5.3	5.2	5.6
$\Delta a$ (1st phase) (m)	0.015	0.016	0.016	0.015	0.015	0.014
$\Delta a$ (2nd phase) (m)	0.039	0.038	0.035	0.039	0.037	0.036
$L_d$ (m)	0.78	0.85	0.91	0.68	0.73	0.79
$k_x$ (1st phase) (–)	0.202	0.195	0.190	0.175	0.168	0.182
$k_x$ (2nd phase) (–)	0.109	0.137	0.102	0.096	0.107	0.125

*Note.*  $c$  is the bar Celerity (i.e., Migration Rate),  $\Delta a$  is the bar Amplitude,  $L_d$  is the Length of the Sediment Deposit, and  $k_x$  is the bar Wavenumber.

#### 4.4. Bar Wavenumber

Results of our analysis suggest that established vegetation decreases the bar wavenumber below the threshold value for incipient meandering, in comparison to bare-bed conditions (Figure 9). The required parameters for the calculations (Equations 2 and 3) were measured from the DEMs and are therefore affected by the precision of these data and their analysis. Furthermore, the measurements of the narrow channel width ( $B_x$  in Figure 3b) relies on the assumption that sediment transport occurs in that channel only. This assumption is consistent with the numerical findings of Jourdain et al. (2020) on eco-morphodynamic simulations of vegetated bars. Additionally, the theory of bar-bend resonance (Blondeaux & Seminara, 1985) relies on the assumptions of one single grain, and it is not available for mixed grain size distribution (see the Appendix A for the full set of equations). Surely, the presence of mixed grain sizes may affect the resonance value, as much as it affects the morphodynamics of alternate bars (Lanzoni & Tubino, 1999) and river meanders (Parker & Andrews, 1985).

Furthermore, the analysis demonstrates that vegetation promotes the planimetric instability of the channel (i.e., *bend stability* according to Blondeaux and Seminara (1985), among others), even with the lower tested density ( $\rho_v = 1,250 \text{ stem m}^{-2}$ , see Table 1). Yet, we must point out that this situation may not occur in real rivers because of the general environmental conditions at the reach scale. Field observations demonstrated that alternate bars often developed following artificial channel straightening (Adami et al., 2016; Serlet et al., 2018). Therefore, vegetation-induced meandering after colonization may take place after construction of restoration projects aimed at both removing artificial levees and allowing the river to move laterally (Figures 1c–1f). In this case, however, the initial channel pattern depends on the flow and sediment supply regime and may not consist of alternate bars (e.g., Eaton et al., 2004; Mueller & Pitlick, 2014). Accordingly, the effects induced by vegetation colonization may differ from those observed in our experiments and must be evaluated on a case-by-case basis. However, it is important to note that vegetation on alternate bars promotes stabilizing effects, which is consistent with previous experimental (e.g., Kyuka et al., 2021; Tal & Paola, 2010) and numerical (e.g., Bertoldi et al., 2014; Jourdain et al., 2020) investigations. Our findings also confirm that vegetation plays a fundamental role in governing the morphodynamic evolution of bar patterns (Rominger et al., 2010; Vargas-Luna et al., 2019), and suggest that vegetation density may be responsible for both local (e.g., sediment deposit) and reach scale (e.g., bar-bend resonance) alterations.

#### 5. Conclusions

In this work, we analyzed the influence of rigid emergent vegetation on the morphodynamics of alternate bars freely developed due to bed instability, later becoming steady hybrid bars. Flume experiments were carried out in a recirculating straight channel and rigid stems were placed only on the highest part of the depositional pattern to mimic the establishment of mature vegetation during low flow periods (e.g., dry season). Results showed that the morphodynamics of the entire flume was affected by the presence of vegetation, despite the fact that plants were deployed in a small area of the channel. Morphodynamic changes occurred in terms of zones subjected to erosion and deposition processes, thus resulting in larger bar amplitude values. Sediment settling downstream of the vegetated patch may suggest migration of vegetated bars, but we showed that such deposits have a finite length and their development may be captured by theoretical relationships available in the literature. This implies

that, in our experiments, vegetated bars elongate, and do not migrate and change in wavelengths. In this regard, the analysis of wavenumbers demonstrated that, after plant deployment, wavenumbers may reach the resonant conditions for planimetric instability toward meandering.

The results of our work give an insight into the interactions between rigid emergent vegetation and morphodynamics, which can have practical implications regarding vegetation management in fluvial corridors. In particular, proper maintenance of in-channel vegetation is required to allow for bar dynamics (migration and growth), and such dynamics may be controlled together with vegetation density. On the contrary, a different river morphodynamic behavior (e.g., lateral migration) may be encouraged when vegetation is allowed to establish and to increase flow diversion. Therefore, proper strategies must be chosen not only according to the species of colonizing plants and the river regime, but also depending on the desired objective of the river restoration project.

### Appendix A: Bar-Bend Resonance

The system of equations for the calculation of the critical conditions for bar-bend resonance is here reported, based on the theory developed by Blondeaux and Seminara (1985). In terms of the longitudinal wavenumber,  $k_x$ , the bar-bend resonance occurs for  $k_x = k_{x,c}$ , where the critical value,  $k_{x,c}$ , can be calculated from the first-order perturbation of the longitudinal flow in phase with the channel curvature, as

$$\Re \left( -d_0[k_x] n - \left( \frac{\lambda_+[k_x] \gamma_+[k_x]}{ik_x} + d_1[k_x] \right) \sinh(\lambda_+[k_x] n) - \left( \frac{\lambda_-[k_x] \gamma_-[k_x]}{ik_x} + d_2[k_x] \right) \sinh(\lambda_-[k_x] n) \right)_{k_x=k_{x,c}} = 0 \quad (A1)$$

where  $\Re(\cdot)$  stands for the real part,  $n$  is the dimensionless transversal coordinate and  $i$  is the imaginary unit. Therein, the functions  $d_0$ ,  $d_1$ , and  $d_2$  are:

$$\left. \begin{aligned} d_0 &= -\frac{\beta_s C + ik_x}{p_2[k_x] - p_1[k_x]} k_x^2 + \frac{ik_x p_3[k_x]}{p_2[k_x] - p_1[k_x]} \frac{G_0[k_x]}{G_2[k_x]} \\ d_1 &= -\frac{\gamma_+[k_x]}{p_2[k_x] - p_1[k_x]} \left( \frac{ik_x p_3[k_x]}{\lambda_+[k_x]} + p_1[k_x] \frac{\lambda_+[k_x]}{ik_x} \right) \\ d_2 &= -\frac{\gamma_-[k_x]}{p_2[k_x] - p_1[k_x]} \left( \frac{ik_x p_3[k_x]}{\lambda_-[k_x]} + p_1[k_x] \frac{\lambda_-[k_x]}{ik_x} \right) \end{aligned} \right\} \quad (A2)$$

respectively. The expressions for  $\lambda_{\pm}$  and  $\gamma_{\pm}$  are as follows:

$$\lambda_{\pm} = \sqrt{\frac{1}{2} \left( -G_1[k_x] \pm \sqrt{G_1^2[k_x] - 4G_2[k_x]} \right)} \quad (A3)$$

$$\gamma_{\pm} = \pm \frac{\lambda_{\pm}^2[k_x] G_0[k_x] / G_2[k_x] + G_3[k_x]}{(\lambda_{\pm}^2[k_x] - \lambda_{\mp}^2[k_x]) \cosh(\lambda_{\pm}[k_x])} \quad (A4)$$

The functions  $G_i$  appearing in Equations A2–A4 combine flow and sediment transport properties and obey the following relationships:

$$\left. \begin{aligned} G_0 &= \frac{\beta_s k_x^3}{p_1[k_x] r \Phi} (p_5[k_x] - p_4[k_x]) (i \beta_s C n - k_x) \\ G_1 &= \frac{\beta_s}{r \Phi} (p_5[k_x] - p_4[k_x]) + \frac{ik_x}{r p_1[k_x]} \left( \beta_s \frac{\theta}{\Phi} \frac{\partial \Phi}{\partial \theta} + F_r^2 p_3[k_x] r + \beta_s \right) - k_x^3 \frac{p_3[k_x]}{p_1[k_x]} \\ G_2 &= -\beta_s \frac{(p_5[k_x] - p_4[k_x]) k_x^2 p_3[k_x]}{p_1[k_x] r \Phi} \\ G_3 &= ik_x \left( \frac{p_2[k_x]}{p_1[k_x]} - 1 \right) \left( \frac{p_0}{r} k_x^2 + F_r^2 \right) + \frac{k_x^3}{p_1[k_x]} (i \beta_s C n - k_x) \end{aligned} \right\} \quad (A5)$$

where it appears  $r$ , the coefficient for lateral sediment transport. The parameter  $p_0$  depends on the turbulence-closure model and lies in the range 7–12. According to Blondeaux and Seminara (1985), we used  $p_0 = 7$ . Finally, the expressions of the additional coefficients  $p_i$  in Equations A2–A5 read:

$$\left. \begin{aligned} p_1 &= ik_x + \beta_s C K_1 \\ p_2 &= \beta_s C (K_2 - 1) \\ p_3 &= ik_x + \beta_s C \\ p_4 &= ik_x K_1 \frac{\theta}{\Phi} \frac{\partial \Phi}{\partial \theta} \\ p_5 &= i \left( \frac{1}{\Phi} \frac{\partial \Phi}{\partial Y} + K_2 \frac{\theta}{\Phi} \frac{\partial \Phi}{\partial \theta} \right) \end{aligned} \right\} \quad (\text{A6})$$

where  $K_1$  and  $K_2$  are two dimensionless coefficients depending on the Chézy coefficient,  $C$ , and the Shields number,  $\theta$ . The expressions for  $K_1$  and  $K_2$  read:

$$\left. \begin{aligned} K_1 &= 2 \left( 1 - \frac{\theta}{C} \frac{\partial C}{\partial \theta} \right)^{-1} \\ K_2 &= \frac{1}{C} \frac{\partial C}{\partial \theta} \left( 1 - \frac{\theta}{C} \frac{\partial C}{\partial \theta} \right)^{-1} \end{aligned} \right\} \quad (\text{A7})$$

respectively.

### Notation

$a$	Frontal area of plants per unit volume
$b$	Degree of non-linearity in sediment transport
$c$	Bar celerity (bar migration rate)
$g$	Acceleration due to gravity
$k_x$	Longitudinal wavenumber
$k_{x,c}$	Longitudinal wavenumber at resonant conditions
$m$	Bar mode
$q_s$	Sediment transport per unit width
$r$	Coefficient for transverse sediment transport
$s$	Bed slope
$t$	Time
$x$	Longitudinal coordinate
$y$	Transverse coordinate
$z$	Vertical coordinate
$\tilde{z}$	Dimensionless vertical coordinate
$A_i$	Amplitude of the $i$ th bar mode from FFT analysis
$B$	Main channel width
$B_s$	Width of the narrow sinuous channel
$C$	Chézy coefficient
$D_{50}$	Mean grain size
$D_n$	Grain size diameter exceeding $n$ percentage
$D_s$	Dimensionless grain size
$D_v$	Vegetation diameter
$Fr$	Froude number
$I$	Sorting index
$L_d$	Length of deposit downstream vegetation patch
$Q$	Flow discharge
$Q_s$	Sediment discharge
$T_1$	Duration of the first (bare-bed) phase
$T_2$	Duration of the second (vegetated) phase
$U$	Flow velocity

$Y$	Water depth
$Y_0$	Normal water depth
$Y_c$	Threshold water depth for sediment transport
$\alpha$	Ratio between longitudinal and transverse adaptations lengths
$\beta$	Aspect ratio (half width-to-depth ratio)
$\beta_{cr}$	Critical aspect ratio for bar formation
$\beta_s$	Aspect ratio of the narrow sinuous channel
$\theta$	Shields number
$\theta_c$	Critical Shields number for sediment transport
$\rho$	Water density
$\rho_s$	Sediment density
$\rho_v$	Vegetation density
$\Delta a$	Bar amplitude (height)
$\Phi$	Dimensionless sediment transport

## Data Availability Statement

Additional material is available at the Zenodo data repository (Calvani et al., 2022).

## Acknowledgments

The authors are grateful to the AE, Dr. Daniel Cadol, Dr. Guido Zolezzi and two additional anonymous reviewers for their comments, which helped to significantly improve the quality of the manuscript. The authors would like to thank the undergraduate and master students who supported the collection of the experimental data. GC thanks Montana Marshall, PE for proofreading the manuscript. Open Access Funding provided by Universita degli Studi di Firenze within the CRUI-CARE Agreement.

## References

- Adami, L., Bertoldi, W., & Zolezzi, G. (2016). Multidecadal dynamics of alternate bars in the Alpine Rhine River. *Water Resources Research*, 52(11), 8938–8955. <https://doi.org/10.1002/2015wr018228>
- Andreotti, B., Claudin, P., Devauchelle, O., Durán, O., & Fourrière, A. (2012). Bedforms in a turbulent stream: Ripples, chevrons and antidunes. *Journal of Fluid Mechanics*, 690, 94–128. <https://doi.org/10.1017/jfm.2011.386>
- Bärenbold, F., Crouzy, B., & Perona, P. (2016). Stability analysis of ecomorphodynamic equations. *Water Resources Research*, 52(2), 1070–1088. <https://doi.org/10.1002/2015wr017492>
- Bennett, S. J., Pirim, T., & Barkdoll, B. D. (2002). Using simulated emergent vegetation to alter stream flow direction within a straight experimental channel. *Geomorphology*, 44(1–2), 115–126. [https://doi.org/10.1016/s0169-555x\(01\)00148-9](https://doi.org/10.1016/s0169-555x(01)00148-9)
- Bentham, T., & Britter, R. (2003). Spatially averaged flow within obstacle arrays. *Atmospheric Environment*, 37(15), 2037–2043. [https://doi.org/10.1016/s1352-2310\(03\)00123-7](https://doi.org/10.1016/s1352-2310(03)00123-7)
- Berends, K. D., Ji, U., Penning, W. E., Warmink, J. J., Kang, J., & Hulscher, S. J. (2020). Stream-scale flow experiment reveals large influence of understory growth on vegetation roughness. *Advances in Water Resources*, 143, 103675. <https://doi.org/10.1016/j.advwatres.2020.103675>
- Bertoldi, W., Gurnell, A., & Drake, N. (2011). The topographic signature of vegetation development along a braided river: Results of a combined analysis of airborne lidar, color air photographs, and ground measurements. *Water Resources Research*, 47(6), 1–13. <https://doi.org/10.1029/2010wr010319>
- Bertoldi, W., Siviglia, A., Tettamanti, S., Toffolon, M., Vetsch, D., & Francalanci, S. (2014). Modeling vegetation controls on fluvial morphological trajectories. *Geophysical Research Letters*, 41(20), 7167–7175. <https://doi.org/10.1002/2014gl061666>
- Bertoldi, W., Welber, M., Gurnell, A., Mao, L., Comiti, F., & Tal, M. (2015). Physical modelling of the combined effect of vegetation and wood on river morphology. *Geomorphology*, 246, 178–187. <https://doi.org/10.1016/j.geomorph.2015.05.038>
- Blondeaux, P., & Seminara, G. (1985). A unified bar–bend theory of river meanders. *Journal of Fluid Mechanics*, 157, 449–470. <https://doi.org/10.1017/s0022112085002440>
- Bywater-Reyes, S., Wilcox, A. C., Stella, J. C., & Lightbody, A. F. (2015). Flow and scour constraints on uprooting of pioneer woody seedlings. *Water Resources Research*, 51(11), 9190–9206. <https://doi.org/10.1002/2014wr016641>
- Calvani, G., Francalanci, S., & Solari, L. (2019). A physical model for the uprooting of flexible vegetation on river bars. *Journal of Geophysical Research: Earth Surface*, 124(4), 1018–1034. <https://doi.org/10.1029/2018jf004747>
- Calvani, G., Francalanci, S., & Solari, L. (2022). Experimental investigations on the effects of vegetation on alternate bars [Dataset]. Zenodo. <https://doi.org/10.5281/zenodo.6469782>
- Calvani, G., Perona, P., Zen, S., Bau', V., & Solari, L. (2019). Return period of vegetation uprooting by flow. *Journal of Hydrology*, 578, 124103. <https://doi.org/10.1016/j.jhydrol.2019.124103>
- Cheng, Y., & da Silva, A. M. F. (2019). Empirical equation for determination of alternate bar height. *Journal of Hydraulic Engineering*, 145(11), 04019037. [https://doi.org/10.1061/\(asce\)jhy.1943-7900.0001633](https://doi.org/10.1061/(asce)jhy.1943-7900.0001633)
- Colombini, M., Seminara, G., & Tubino, M. (1987). Finite-amplitude alternate bars. *Journal of Fluid Mechanics*, 181(1), 213–232. <https://doi.org/10.1017/s0022112087002064>
- Colombini, M., & Stocchino, A. (2011). Ripple and dune formation in rivers. *Journal of Fluid Mechanics*, 673, 121–131. <https://doi.org/10.1017/s0022112011000048>
- Crosato, A., Desta, F. B., Cornelisse, J., Schuurman, F., & Uijtewaal, W. S. (2012). Experimental and numerical findings on the long-term evolution of migrating alternate bars in alluvial channels. *Water Resources Research*, 48(6), W06524. <https://doi.org/10.1029/2011wr011320>
- Crosato, A., & Mosselman, E. (2009). Simple physics-based predictor for the number of river bars and the transition between meandering and braiding. *Water Resources Research*, 45(3), W05415. <https://doi.org/10.1029/2008wr007242>
- Crosato, A., & Mosselman, E. (2020). An integrated review of river bars for engineering, management and transdisciplinary research. *Water*, 12(2), 596. <https://doi.org/10.3390/w12020596>
- Defina, A. (2003). Numerical experiments on bar growth. *Water Resources Research*, 39(4), 1092. <https://doi.org/10.1029/2002wr001455>
- Duró, G., Crosato, A., & Tassi, P. (2016). Numerical study on river bar response to spatial variations of channel width. *Advances in Water Resources*, 93, 21–38. <https://doi.org/10.1016/j.advwatres.2015.10.003>

- Eaton, B. C., Church, M., & Millar, R. G. (2004). Rational regime model of alluvial channel morphology and response. *Earth Surface Processes and Landforms*, 29(4), 511–529. <https://doi.org/10.1002/esp.1062>
- Engelund, F. (1970). Instability of erodible beds. *Journal of Fluid Mechanics*, 42(2), 225–244. <https://doi.org/10.1017/s0022112070001210>
- Federici, B., & Seminara, G. (2006). Effect of suspended load on sandbar instability. *Water Resources Research*, 42(7), W07407. <https://doi.org/10.1029/2005wr004399>
- Follett, E. M., & Nepf, H. M. (2012). Sediment patterns near a model patch of reedy emergent vegetation. *Geomorphology*, 179, 141–151. <https://doi.org/10.1016/j.geomorph.2012.08.006>
- Francalanci, S., Solari, L., Toffolon, M., & Parker, G. (2012). Do alternate bars affect sediment transport and flow resistance in gravel-bed rivers? *Earth Surface Processes and Landforms*, 37(8), 866–875. <https://doi.org/10.1002/esp.3217>
- Garcia, M., & Niño, Y. (1993). Dynamics of sediment bars in straight and meandering channels: Experiments on the resonance phenomenon. *Journal of Hydraulic Research*, 31(6), 739–761. <https://doi.org/10.1080/00221689309498815>
- Gurnell, A. M., Bertoldi, W., & Corenblit, D. (2012). Changing river channels: The roles of hydrological processes, plants and pioneer fluvial landforms in humid temperate, mixed load, gravel bed rivers. *Earth-Science Reviews*, 111(1), 129–141. <https://doi.org/10.1016/j.earscirev.2011.11.005>
- Halliday, D., Resnick, R., & Walker, J. (2013). *Fundamentals of physics*. John Wiley & Sons.
- Hortobágyi, B., Corenblit, D., Steiger, J., & Peiry, J.-L. (2018). Niche construction within riparian corridors. Part I: Exploring biogeomorphic feedback windows of three pioneer riparian species (Allier River, France). *Geomorphology*, 305, 94–111. <https://doi.org/10.1016/j.geomorph.2017.08.048>
- Ikedda, S. (1984). Prediction of alternate bar wavelength and height. *Journal of Hydraulic Engineering*, 110(4), 371–386. [https://doi.org/10.1061/\(asce\)0733-9429\(1984\)110:4\(371\)](https://doi.org/10.1061/(asce)0733-9429(1984)110:4(371))
- Jourdain, C., Claude, N., Tassi, P., Cordier, F., & Antoine, G. (2020). Morphodynamics of alternate bars in the presence of riparian vegetation. *Earth Surface Processes and Landforms*, 45(5), 1100–1122. <https://doi.org/10.1002/esp.4776>
- Kleinhaus, M. G., van Dijk, W. M., van de Lageweg, W. I., Hoyal, D. C., Markies, H., van Maarseveen, M., et al. (2014). Quantifiable effectiveness of experimental scaling of river-and delta morphodynamics and stratigraphy. *Earth-Science Reviews*, 133, 43–61. <https://doi.org/10.1016/j.earscirev.2014.03.001>
- Kyuka, T., Yamaguchi, S., Inoue, Y., Arnez Ferrel, K. R., Kon, H., & Shimizu, Y. (2021). Morphodynamic effects of vegetation life stage on experimental meandering channels. *Earth Surface Processes and Landforms*, 46(7), 1225–1237. <https://doi.org/10.1002/esp.5051>
- Lanzoni, S. (2000a). Experiments on bar formation in a straight flume: 1. Uniform sediment. *Water Resources Research*, 36(11), 3337–3349. <https://doi.org/10.1029/2000wr900160>
- Lanzoni, S. (2000b). Experiments on bar formation in a straight flume: 2. Graded sediment. *Water Resources Research*, 36(11), 3351–3363. <https://doi.org/10.1029/2000wr900161>
- Lanzoni, S., & Tubino, M. (1999). Grain sorting and bar instability. *Journal of Fluid Mechanics*, 393, 149–174. <https://doi.org/10.1017/s0022112099005583>
- Lisle, T. E., Ikeda, H., & Iseya, F. (1991). Formation of stationary alternate bars in a steep channel with mixed-size sediment: A flume experiment. *Earth Surface Processes and Landforms*, 16(5), 463–469. <https://doi.org/10.1002/esp.3290160507>
- Melville, B., & Sutherland, A. (1988). Design method for local scour at bridge piers. *Journal of Hydraulic Engineering*, 114(10), 1210–1226. [https://doi.org/10.1061/\(asce\)0733-9429\(1988\)114:10\(1210\)](https://doi.org/10.1061/(asce)0733-9429(1988)114:10(1210))
- Morgan, J. A., Brogan, D. J., & Nelson, P. A. (2017). Application of structure-from-motion photogrammetry in laboratory flumes. *Geomorphology*, 276, 125–143. <https://doi.org/10.1016/j.geomorph.2016.10.021>
- Mueller, E. R., & Pitlick, J. (2014). Sediment supply and channel morphology in mountain river systems: 2. Single thread to braided transitions. *Journal of Geophysical Research: Earth Surface*, 119(7), 1516–1541. <https://doi.org/10.1002/2013jf003045>
- Nelson, P. A., & Morgan, J. A. (2018). Flume experiments on flow and sediment supply controls on gravel bedform dynamics. *Geomorphology*, 323, 98–105. <https://doi.org/10.1016/j.geomorph.2018.09.011>
- Nepf, H. M. (2012). Hydrodynamics of vegetated channels. *Journal of Hydraulic Research*, 50(3), 262–279. <https://doi.org/10.1080/00221686.2012.696559>
- Parker, G., & Andrews, E. (1985). Sorting of bed load sediment by flow in meander bends. *Water Resources Research*, 21(9), 1361–1373. <https://doi.org/10.1029/wr021i009p01361>
- Perona, P., & Crouzy, B. (2018). Resilience of riverbed vegetation to uprooting by flow. *Proceedings of the Royal Society A*, 474(2211), 20170547. <https://doi.org/10.1098/rspa.2017.0547>
- Redolff, M., Zolezzi, G., & Tubino, M. (2019). Free and forced morphodynamics of river bifurcations. *Earth Surface Processes and Landforms*, 44(4), 973–987. <https://doi.org/10.1002/esp.4561>
- Rodrigues, S., Claude, N., Juge, P., & Breheret, J.-G. (2012). An opportunity to connect the morphodynamics of alternate bars with their sedimentary products. *Earth Surface Processes and Landforms*, 37(2), 240–248. <https://doi.org/10.1002/esp.2255>
- Rominger, J. T., Lightbody, A. F., & Nepf, H. M. (2010). Effects of added vegetation on sand bar stability and stream hydrodynamics. *Journal of Hydraulic Engineering*, 136(12), 994–1002. [https://doi.org/10.1061/\(asce\)hy.1943-7900.0000215](https://doi.org/10.1061/(asce)hy.1943-7900.0000215)
- Rominger, J. T., & Nepf, H. M. (2011). Flow adjustment and interior flow associated with a rectangular porous obstruction. *Journal of Fluid Mechanics*, 680, 636–659. <https://doi.org/10.1017/jfm.2011.199>
- Schirmer, M., Luster, J., Linde, N., Perona, P., Mitchell, E. A., Barry, D. A., et al. (2014). Morphological, hydrological, biogeochemical and ecological changes and challenges in river restoration—The Thur river case study. *Hydrology and Earth System Sciences*, 18(6), 2449–2462. <https://doi.org/10.5194/hess-18-2449-2014>
- Seminara, G., & Tubino, M. (1992). Weakly nonlinear theory of regular meanders. *Journal of Fluid Mechanics*, 244(1), 257–288. <https://doi.org/10.1017/s0022112092003069>
- Serlet, A. J., Gurnell, A. M., Zolezzi, G., Wharton, G., Belleudy, P., & Jourdain, C. (2018). Biomorphodynamics of alternate bars in a channelized, regulated river: An integrated historical and modelling analysis. *Earth Surface Processes and Landforms*, 43(9), 1739–1756. <https://doi.org/10.1002/esp.4349>
- Shimada, R., Shimizu, Y., Hasegawa, K., & Iga, H. (2013). Linear stability analysis on the meander formation originated by alternate bars. *JSCE Journal of Hydraulic Engineering*, 69(Pt 4), 1147. [https://doi.org/10.2208/jscejhe.69.i\\_1147](https://doi.org/10.2208/jscejhe.69.i_1147)
- Solari, L., Van Oorschot, M., Belletti, B., Hendriks, D., Rinaldi, M., & Vargas-Luna, A. (2016). Advances on modelling riparian vegetation—Hydromorphology interactions. *River Research and Applications*, 32(2), 164–178. <https://doi.org/10.1002/rra.2910>
- Tal, M., & Paola, C. (2010). Effects of vegetation on channel morphodynamics: Results and insights from laboratory experiments. *Earth Surface Processes and Landforms*, 35(9), 1014–1028. <https://doi.org/10.1002/esp.1908>
- Tubino, M. (1991). Growth of alternate bars in unsteady flow. *Water Resources Research*, 27(1), 37–52. <https://doi.org/10.1029/90wr01699>

- Tubino, M., & Seminara, G. (1990). Free–forced interactions in developing meanders and suppression of free bars. *Journal of Fluid Mechanics*, 214(1), 131–159. <https://doi.org/10.1017/s0022112090000088>
- van de Lageweg, W. I., Van Dijk, W. M., Baar, A. W., Rutten, J., & Kleinhans, M. G. (2014). Bank pull or bar push: What drives scroll-bar formation in meandering rivers? *Geology*, 42(4), 319–322. <https://doi.org/10.1130/g35192.1>
- Vargas-Luna, A., Crosato, A., Calvani, G., & Uijttewaal, W. S. (2016). Representing plants as rigid cylinders in experiments and models. *Advances in Water Resources*, 93, 205–222. <https://doi.org/10.1016/j.advwatres.2015.10.004>
- Vargas-Luna, A., Duró, G., Crosato, A., & Uijttewaal, W. (2019). Morphological adaptation of river channels to vegetation establishment: A laboratory study. *Journal of Geophysical Research: Earth Surface*, 124(7), 1981–1995. <https://doi.org/10.1029/2018jfe004878>
- Venditti, J., Nelson, P., Minear, J., Wooster, J., & Dietrich, W. (2012). Alternate bar response to sediment supply termination. *Journal of Geophysical Research*, 117(F2), 2039. <https://doi.org/10.1029/2011jfe002254>
- Vignoli, G., & Tubino, M. (2004). Le condizioni di emersione di macro forme di fondo in alvei in ghiaia. In *29° Convegno di idraulica e costruzioni idrauliche. Trento, Italy* (pp. 563–570).
- Wong, M., & Parker, G. (2006). Reanalysis and correction of bed-load relation of Meyer-Peter and Müller using their own database. *Journal of Hydraulic Engineering*, 132(11), 1159–1168. [https://doi.org/10.1061/\(asce\)0733-9429\(2006\)132:11\(1159\)](https://doi.org/10.1061/(asce)0733-9429(2006)132:11(1159))
- Yalin, M. S. (1992). *River mechanics*. Pergamon.
- Yamasaki, T. N., Jiang, B., Janzen, J. G., & Nepf, H. M. (2021). Feedback between vegetation, flow, and deposition: A study of artificial vegetation patch development. *Journal of Hydrology*, 598, 126232. <https://doi.org/10.1016/j.jhydrol.2021.126232>
- Zen, S., Zolezzi, G., & Tubino, M. (2014). A theoretical analysis of river bars stability under changing channel width. *Advances in Geosciences*, 39, 27–35. <https://doi.org/10.5194/adgeo-39-27-2014>
- Zolezzi, G., Guala, M., Termini, D., & Seminara, G. (2005). Experimental observations of upstream overdeepening. *Journal of Fluid Mechanics*, 531, 191–219. <https://doi.org/10.1017/s0022112005003927>
- Zong, L., & Nepf, H. (2010). Flow and deposition in and around a finite patch of vegetation. *Geomorphology*, 116(3), 363–372. <https://doi.org/10.1016/j.geomorph.2009.11.020>
- Zong, L., & Nepf, H. (2011). Spatial distribution of deposition within a patch of vegetation. *Water Resources Research*, 47(3), W03516. <https://doi.org/10.1029/2010wr009516>